

Measurement System for Full Three-Dimensional Motion Characterization of MEMS

Christian Rembe and Richard S. Muller, *Life Fellow, IEEE*

Abstract—Advanced testing methods for the dynamics of mechanical microdevices are necessary to develop reliable, marketable microelectromechanical systems (MEMS). A key purpose for mechanically testing MEMS is to provide feedback of measurements that can help the designer progress in an iterative process from prototypes to fully developed products. The effectiveness of these procedures is markedly enhanced if the measurements include high-speed dynamic visualizations of mechanical structures in the microsystem. These data can be obtained using a measurement system that is capable of stroboscopic imaging, interferometry, and digital-image processing. We present such a system and demonstrate its capabilities in three disparate MEMS applications: a gimballed microactuator built for a miniaturized magnetic-disk information-storage system; a micromirror array for an adaptive-optics system; and a microgyroscope that can be applied in a number of microsystems. [794]

Index Terms—Design evaluation, image processing, interferometry, MEMS characterization, MEMS reliability, MEMS testing.

I. INTRODUCTION

MEMS are typically characterized by observing the system output when a defined input is applied. For example, in the case of an electrostatic actuator with an integrated sensor the input driving voltage is compared with a signal from the capacitive sensor that is representative of the actuator displacement. Static characteristics as well as the frequency-response behavior can be investigated using this method and, theoretically at least, full time-response information can be extracted using Fourier analysis. Proceeding in this way is tedious and the results are inferential. Direct observation of dynamic behavior can speed-up the characterization process and, at the same time, make evident possible nonlinear effects including those caused by aging [1].

One way to measure out-of-plane movements is with a commercially available scanning Laser-Doppler Vibrometer (MSV 300, Micro-Scanning Vibrometer) from Polytec PI [2]–[4]. The Polytec system measures the velocity of a moving surface by detecting the Doppler frequency shift of a reflected laser beam.

Manuscript received January 4, 2002; revised March 11, 2002. C. Rembe has been a Lynen Fellow supported by the Alexander von Humboldt-Foundation. This work was supported in part by the BSAC industrial members, the National Science Foundation Science and Technology Center for Adaptive Optics, managed by the University of California at Santa Cruz under cooperative agreement AST-9876783, and DARPA. Subject Editor N. de Rooij.

C. Rembe was with the Berkeley Sensor and Actuator Center, University of California at Berkeley, 497 Cory Hall, Berkeley, CA 93720. He is now with Polytec GmbH, D-76337 Waldbronn, Germany (e-mail: c.rembe@polytec.de).

R. S. Muller is with the Berkeley Sensor and Actuator Center, University of California at Berkeley, Berkeley, CA 93720 USA (e-mail: muller@eecs.berkeley.edu).

Digital Object Identifier 10.1109/JMEMS.2002.803285.

The displacement at a single spot of the surface under investigation is computed by integrating the velocity measurement. By scanning a 1 mW continuous-wave (cw) laser beam over the surface, the system measures the vibration of an area that a user preselects using a graphical user interface.

Pure out-of-plane motions can also be measured with a Stroboscopic Interferometer System (SIS) developed by Hart *et al.* at the Berkeley Sensor and Actuator Center (BSAC) [5], [6]. However, neither the SIS nor the MSV are capable of measuring in-plane motion. Therefore, mechanical in-plane vibration modes that are coupled to the out-of-plane-deflections cannot be investigated with these systems.

In-plane motions of MEMS can, however, be studied using the Computer Microvision System (CMS), a stroboscopic microscope that has been developed at MIT [7], [8]. In the CMS, periodic motions of a microstructure that are imaged with a microscope on a charge-coupled device (CCD) camera are frozen using a high-speed strobed light source. By processing the measured data with digital-image-processing algorithms, the CMS can recover in-plane motions from the captured images and, by employing an additional focus system, the CMS is also able to extract the out-of-plane motions. Two limitations in the CMS out-of-plane-measurement method are that the moving element must not deform in order for the measurement to be valid, and also that the resolution of the measurement is appreciably poorer than that obtainable using interferometric methods. Improvements in the CMS that overcome the resolution problem have recently been described by the MIT group [9]. In the newer system the in-plane motions are extracted through data processing in which the interferometrically produced fringe patterns due to out-of-plane motions are mathematically removed before an image-processing algorithm is employed. Rigid-body motions are computed point-by-point in user-selected regions on the device surface with high resolution (2.5 nm in-plane, <1 nm out-of-plane). Deformations that may occur in the measurement region during the motion cannot be detected by this method.

A system for the investigation of not-repeated, transient processes has been developed at the University of Ulm [10]–[12]. In this system a high-speed camera is combined with a special light source and an optical microscope to form a High-Speed Motion Analyzer (HSMA). The Ulm University system can resolve in-plane, but not out-of-plane, motions of mechanical and fluidic MEMS devices.

In this paper we describe a new experimental method that allows the measurement of out-of-plane deflections together with in-plane-rigid-body motions of microstructures in a single experiment. The new system combines the out-of-plane deforma-

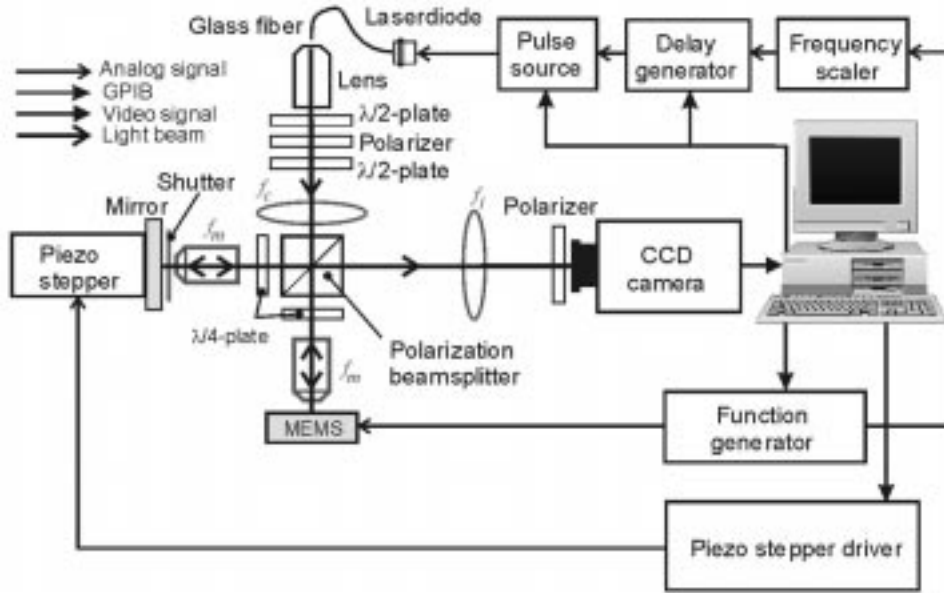


Fig. 1. Schematic of stroboscopic interferometer system. The abbreviations used are as follows: L — $\lambda/2$ —wave-plate, P —polarizer, PBS —polarization beam splitter, f_c —condenser lens, f_i —imaging lens, and f_m —microscope objective for imaging, LD —laser diode, M —reference mirror

tion-measurement capability demonstrated for the BSAC SIS with a new in-plane-motion-measurement feature.

II. STROBOSCOPIC MICROSCOPIC INTERFEROMETER

Our work on a system for dynamic measurements of microstructures in three dimensions is based upon improvements to the earlier BSAC SIS system [5], which used stroboscopic interferometric methods for highly precise measurements of out-of-plane motions.

In the new system, a pulsed-laser diode with a wavelength $\lambda = 688$ nm provides a strobed light source to “freeze” the motion of a periodically moving microstructure. The laser light is coupled into a mono-mode fiber to filter astigmatism from the beam and the other end of the fiber is placed in the focus of a microscope objective to form a collimated laser beam. A $\lambda/2$ -plate, placed after the microscope objective (see Fig. 1), rotates the polarized beam which then enters a polarization-beam splitter that parcels it into two perpendicular directions and also polarizes the beams perpendicularly. This arrangement allows the adjustment of constant polarization for an optimum illumination power. The intensities of both beams can be adjusted by rotating the $\lambda/2$ -plate making it possible to compensate the differences of the reflectances between the sample and the reference mirror. The $\lambda/4$ -plates between, respectively, the beam-splitter-and-the-reference mirror, and the beam-splitter-and-the-object ensure that both beams are directed onto a CCD sensor instead of returning to the source. We have integrated the linear progressive-scan camera “6600 from Cohu” in our setup. The beam path of the lighting is adjusted through the lens focus lengths f_i , f_c , and f_m according to the rules of Köhler to insure a high contrast of the images. By choosing different focus lengths for f_m , magnification, resolution, depth-of-focus, and

field-of-view can all be adjusted. We use four different objectives having magnifications $5\times$, $10\times$, $20\times$, and $40\times$ (objective lenses from Zeiss).

To visualize the typically very tiny mechanical structures used in MEMS, a microscope objective (f_m) having a large numerical aperture (NA) must be placed between the beam splitter and the specimen. The distance from the specimen to the microscope objective has to be the focal length of the objective to image the specimen to infinity. The lens with focal length f_i is placed between the beam splitter and the light sensor to create an imaging system consisting of this lens and the microscope objective. The distance between the lens and the CCD sensor is the focal length f_i . Then, for a $10\times$ microscope objective (Zeiss Epiplan, $NA = 0.25$) the magnification m of this imaging system is

$$m = \frac{f_i}{f_m} \approx 8 \quad (1)$$

where $f_m = 18.7$ mm and $f_i = 150$ mm. The CCD pixels have a size of $9.9 \mu\text{m} \times 9.9 \mu\text{m}$. Therefore, for $m \approx 8$, a pixel of the specimen image corresponds to an area of approximately $1.24 \mu\text{m} \times 1.24 \mu\text{m}$. The image-pixel size has to be calibrated before a precise in-plane-motion analysis can be performed. We use a camera as a light sensor to register the image of the specimen. The optical path of the reference beam has to be the same as that of the measurement beam, which requires us to insert a second microscope objective with the same focal length f_m between the reference mirror and the beam splitter.

A lens with focus length f_c is placed between the half-wave-plate and the beam splitter so that a defined area of the MEMS surface is illuminated through this lens (f_c) and the microscope objective (f_m). The lens and the microscope objective image a cross section of the collimated laser beam on the imaged area of the specimen and the reference mirror. The diameter of the

illuminated area on the specimen and the reference mirror d_i is defined through the diameter of the collimated beam $d_c = 6$ mm, the focus length $f_c = 125$ mm, and the focal length f_m . For the Zeiss 10 \times Epiplan objective d_i results in

$$d_i = \frac{f_m}{f_c} d_c \approx 900 \mu\text{m}. \quad (2)$$

The diameter of the light spot on the imaging plane at the CCD sensor d_s is calculated through

$$d_s = \frac{f_i}{f_m} d_i \approx 7.2 \text{ mm}. \quad (3)$$

The diameter d_i is independent from f_m , as is obvious when combining (3) and (2). The area of the chip (6.5 mm \times 4.9 mm) is smaller than the image of the illuminated area of the object imaged through the microscope objective f_m and the lens f_i on the image plane at the chip. The illuminated area is just large enough as it is necessary to achieve a homogeneous illumination for the area captured by the CCD sensor. The numerical apertures of the illumination and imaging lenses are, for our arrangement, the same. Therefore, the beam path is adjusted using the rules of Köhler [13] so that a high contrast of the images and adequate optimal illumination power is ensured.

The interferometer corresponds to a Twyman–Green arrangement [14] of a modified Michelson interferometer. The special configuration with two microscope objectives as we use it in our setup is known as a Linnik interferometric [14] objective.

The interferometer forms an image of the MEMS device that is crossed by bright and dark fringes, which can be interpreted as a contour map of object surface heights. To measure the shape of a static specimen or that of a moving specimen, “frozen” by the strobe light, phase-shifting interferometry (PSI) is used. A five-step PSI algorithm in which the fringe pattern of a specimen is visualized five times for five different reference-mirror positions is employed. Finally, the surface-height map is calculated with self-developed analyzing software.

The system described in the foregoing can also be used as common light microscope if the light path to the reference mirror is removed. The schematic of the system when this is done [which we call a Stroboscopic Microscopic Interferometer System (SMIS)] is shown in Fig. 1. The SMIS becomes a conventional light microscope when the light beam that goes to the reference mirror is shadowed with shutter S . Through the stroboscopic, visible-light illumination, a set (*set 1*) of images is taken of the periodic motion without forming interference patterns. We have developed a new algorithm to extract the in-plane motion from this sequence with subpixel resolution. After the system has taken a set (*set 1*) of images without interference fringes, the shutter is moved out of the laser beam making it an interferometer. In this configuration, a set (*set 2*) of images that contain the interference pattern is taken. The translation data extracted from *set 1* are then used to recalculate the in-plane motion from the images of *set 2*. *Set 2* contains five images for every single time point at which the surface-height map is measured because of the five-step-PSI method that we apply. This procedure has already been used for the earlier SIS and is described in reference [5].

Therefore, to investigate the three-dimensional (3-D) deflection at 10 time points the SMIS saves 10 images for the in-plane-

motion extraction and 5×10 images for the out-of-plane-motion computation. Therefore, a full sequence for a measurement at 10 time points contains 60 images. The analysis software, which computes full three-dimensional motion, is written with MATLAB.¹

The strobe-phase delay is altered automatically during the measurement routine to perform a deflection measurement over one full cycle of a periodic motion. In order to perform accurate time measurements at frequencies as high as 1 MHz the strobe-phase delay and the width of the strobe pulse have to be well defined. To accomplish this goal we use the synchronization TTL-output of the function generator (33120A from Agilent Technologies) as a clock for the experiment. The function generator also supplies the driving signal for the MEMS device as well as a synchronization signal that triggers the delay generator (DG535 from Stanford Research Systems, Inc.). The delay generator triggers the pulse generator for the laser diode and increases the strobe-phase delay during the automated measurement procedure with picosecond resolution (5 ps).

The maximum device-dependent repetition rate ν_r of the delay generator is $\nu_r = 1/(1 \mu\text{s} + \delta_{\text{max}})$. Here, δ_{max} is the longest delay applied during the automated measurement procedure. This limits the maximum frequency that can be investigated because the longest strobe-phase delay depends on the driving frequency of the MEMS device. For example, only the first π radians in phase can be investigated at 500 kHz ($\delta_{\text{max}} = 1 \mu\text{s}$). We improved upon this limitation by dividing the TTL synchronization signal of the function generator with a frequency scaler, $\nu_r = 1/2\nu$. The frequency scaler is realized with the digital counter (SN74LS162N from Texas Instruments). Less light is integrated by the image sensor as result, but this is only important for low repetition frequencies. Therefore, for low repetition rates (MEMS driving frequencies $\nu < 10$ kHz) we switch the scaler off ($\nu_r = \nu$) and the limitation for δ_{max} is valid. The limitation of the delay generator is less important at lower frequencies ($\delta_{\text{max}} = 1/\nu - 1 \mu\text{s} \approx 1/\nu$ for $\nu < 10$ kHz). The current pulse for the laser diode is generated by the precision current source (LDP-3840 from ILX Lightwave) and can be chosen to have any value between 100 ns and 10 μs . We use the laser diode (ML1013R from Mitsubishi) as light source.

III. ANALYSIS SOFTWARE

We have developed a new algorithm to extract the in-plane motion from an image sequence (*set 1*) with a sub-pixel resolution. The structure of the new combined algorithm to compute full three-dimensional motion is presented in Fig. 2. The Analysis software is written with MATLAB.

A. Algorithm for In-Plane-Motion Computation

The user has to specify two regions in the first image of *set 1* (*image 1*) before the in-plane displacement can be calculated. The first region defines the region for the in-plane algorithm. The second region has to be inside the region for the algorithm (ROA) and is termed in Fig. 3 as the region of interest (ROI). The ROI must be a part of *image 1* that shows only the moving

¹The MathWorks, Inc., Natick, MA.

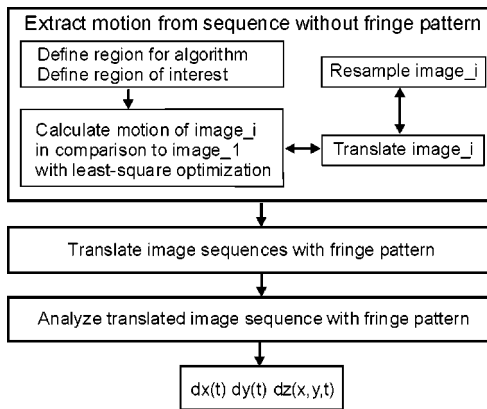


Fig. 2. Structure of the analysis software.

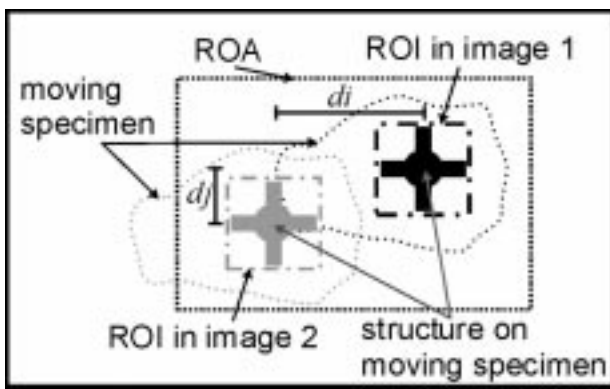
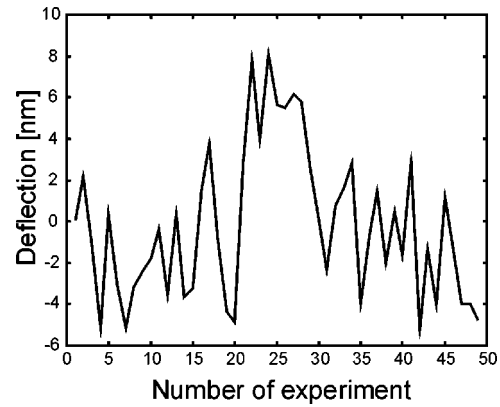


Fig. 3. Definition and restriction of ROA and ROI.

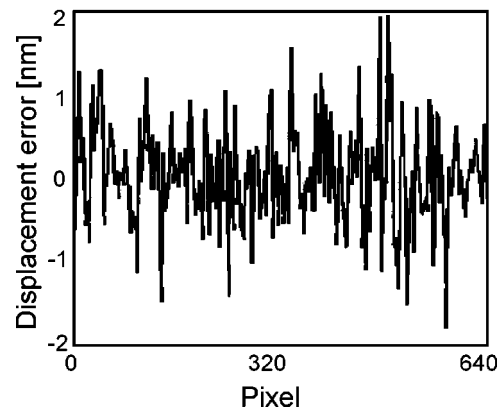
structure. The algorithm can only work properly if the structure of the image part in ROI is not deformed somewhere in the ROA of the remaining images of *set 1*. This is the demand on the definition of ROA that must be ensured by the user. If ROA is oversized, the computation time increases unnecessarily. In the following, the algorithm for in-plane computation is explained on the example of two images in *set 1*. The restrictions for the definition of ROA and ROI are specified in Fig. 3. For in-plane motion SMIS can only measure rigid-body motion. The reason for this restriction is that the algorithm can only calculate the in-plane-translation motion of a not deformed structure on the moving specimen in ROI.

In the following we number the column of each picture with i_n and the rows with $j_n(i_n, j_n \in \mathbb{N})$. The initial row (number $j_n = 1$) is the bottom row of ROI. Column number $i_n = 1$ is the first column at the left side of ROI [15]. The advantage of these definitions is that we can define a coordinate system i and $j(i, j \in \mathbb{R})$ that coincides for integer values with the numbers of the columns i_n and rows j_n . The displacements d_i and d_j in Fig. 3 are computed using digital-image-processing methods. The progressive-scan-CCD 6600 (from Cohu) camera captures 8 bit gray-level images that are saved as TIF-files on the hard disk. The TIF files are transformed to matrices by MATLAB.

In digital-image processing, an image is defined as the continuous gray-level-distribution function $I(i, j)$ that would be produced by an image sensor having infinitely small pixels with the



(a)



(b)

Fig. 4. Typical (a) in-plane noise measurement and (b) out-of-plane noise measurement.

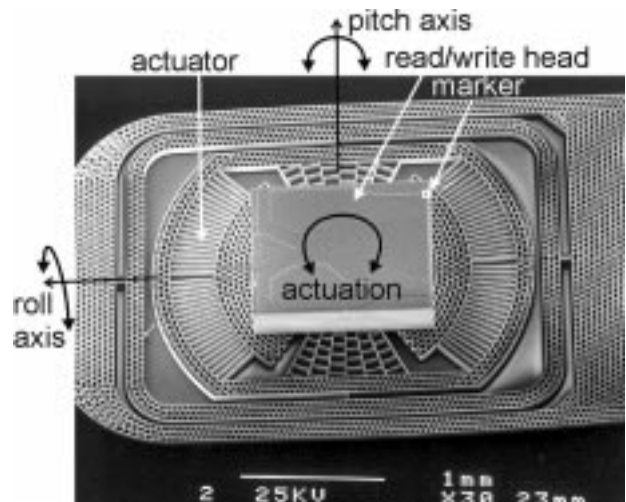


Fig. 5. SEM photograph of gimbaled microactuator (courtesy Lilac Muller).

same sensitivity as those in the CCD camera [15]. We use this definition for the *image* in the following.

Thus, the sampled-image-matrix \underline{M} with the components $I_s(i_n, j_n)$ is the TIF-image or MATLAB matrix and the resampled image $I_r(i, j)$ is the continuous gray-level-distribution function that can be calculated from the sampled image by employing the Nyquist Sampling Theorem. The formulation

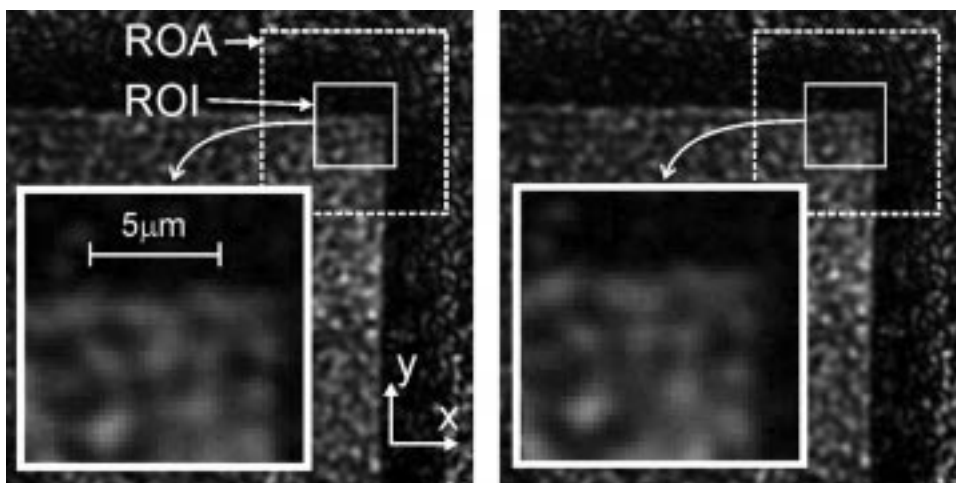


Fig. 6. Images of set 1 at (a) $\pi/2$ and (b) $3\pi/2$ rad delay in respect to the input signal. The region of interest (ROI) is zoomed.

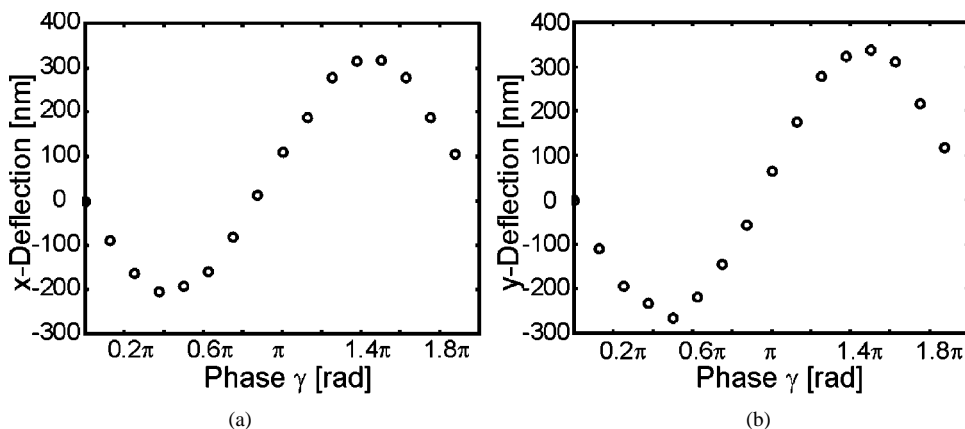


Fig. 7. In-plane-motion at 1250 kHz: (a) x and (b) y deflection.

for a sampled image with n columns and m rows is shown as follows:

$$F(i, l) = \sum_{k=1}^n \frac{\sin(\pi(k-i))}{\pi(k-i)} I_s(k, j_n)$$

$$I_r(i, j) = \sum_{l=1}^m \frac{\sin(\pi(l-j))}{\pi(l-j)} F(i, l)_i. \quad (4)$$

One well-known problem in resampling of signals is that of aliasing which happens when the highest frequency in a signal ν_N is more than half of the sampling frequency ν_S

$$\nu_N > \frac{1}{2} \nu_S. \quad (5)$$

In this condition, high-frequency information is *aliased* to appear as low-frequency information. This problem can be automatically avoided if the image resolution ρ_i is adjusted such that $\rho_i = 0.61\lambda/NA$, and the CCD-pixel resolution $\rho_p = mp_s(p_s = 9.9 \mu\text{m}$ is the CCD-pixel size) are designed so that $\rho_i > 2\rho_p$. These rules govern choices for the numerical aperture NA , magnification m , and pixel size of the CCD chip.

The in-plane-motion algorithm calculates the shifts di and dj between *image 1* (I_1) and *image 2* (I_2) through least-square-optimization

$$\min(\|I_{1,s}(i_n, j_n) - I_{2,r}(i_n - di, j_n - dj)\|_2) \quad (6)$$

where

$$\|A(k, l)\|_2 = \sqrt{\sum_{k,l} A_{k,l}^2} \quad (7)$$

is the L_2 norm [16]. The least-square problem in (6) is solved by employing the Nelder–Mead algorithm [17] that is implemented in MATLAB. This algorithm is very robust in finding the global optimum so that displacements over several pixels are calculated with subpixel resolution. In-plane-rotational computation can also be implemented with this method using the operation

$$\begin{bmatrix} i_{n,2} \\ j_{n,2} \end{bmatrix} = \begin{bmatrix} \cos \varphi & \sin \varphi \\ -\sin \varphi & \cos \varphi \end{bmatrix} \begin{bmatrix} i_{n,1} - c_i \\ j_{n,1} - c_j \end{bmatrix} + \begin{bmatrix} c_i \\ c_j \end{bmatrix} \quad (8)$$

with the fulcrum c and the rotation angle φ .

Direct employment of these methods is infeasible for typical computers because the computation time for image translation and rotation (even for small ROI's) is too long [an example is half an hour for the data shown in Fig. 7 even when linear interpolation is used instead of (4)]. Therefore, gradient-based methods [7] or frequency-domain methods [18] are usually used to estimate displacement between images.

We have developed an algorithm that translates and resamples an image with linear interpolation in one step. The restriction for this algorithm is that rotations in ROI cannot be computed. The

algorithm contains a function to shift the columns of a sampled image \underline{M}

$$\underline{c}_{i, \text{new}} = \underline{c}_{i+1, \text{old}}, \quad \underline{c}_{i, \text{new}} = \underline{c}_{i-1, \text{old}} \quad (9)$$

to the left or to the right, respectively. Here $\underline{c}_{i, \text{new}}$ is the i_n column after the column shift and $\underline{c}_{i\pm 1, \text{old}}$ the $i_n \pm 1$ column before the shifting. All entries in the left column \underline{c}_1 of a new right-shifted matrix are set to zero. The right column of the matrix before the right shifting vanishes because the image size remains the same. The inverse occurs for a shift to the left. The image matrix can be shifted up and down in the same way

$$\underline{r}_{i, \text{new}} = \underline{r}_{i+1, \text{old}}, \quad \underline{r}_{i, \text{new}} = \underline{r}_{i-1, \text{old}} \quad (10)$$

where \underline{r}_i is the i_n row.

Therefore, the images can be shifted full pixels by employing (9) and (10). Shifts with subpixel resolution are performed with linear combinations of full-pixel-shifted matrixes. If we define a matrix \underline{M}_k that is right-shifted k pixels by employing operation (9), a subpixel-resolution shift of $i \in \mathbb{R}$, $i \geq 0$ pixels to the right is expressed by

$$\underline{M}_i = (i - k) \underline{M}_{k+1} + (k + 1 - i) \underline{M}_k \quad (11)$$

where k is the largest integer that is smaller than i ($(i - k) < 1$). Respectively, a shift to the left about $i \leq 0$ pixel is defined by

$$\underline{M}_i = (k - i) \underline{M}_{k-1} + (1 + i - k) \underline{M}_k \quad (12)$$

where k is the smallest integer that is greater than i . The equations for a shift up or down about $j \in \mathbb{R}$ pixel are counterpart equations to (11) and (12). The shifting algorithm given by (11) and (12) employs automatically a linear approximation between the pixels as the resample method. The distance between two pixels is 1. For linear approximation between two pixels at k and $k + 1$ with the values $F(k)$ and $F(k + 1)$ the relation

$$\begin{aligned} F(i) &= F(k) + \frac{F(k+1) - F(k)}{k+1-k} (i - k) \\ &= (i - k)F(k+1) + (k + 1 - i)F(k) \end{aligned} \quad (13)$$

is valid. The comparison of (13) with (11) proves the statement of linear approximation.

There are two possibilities to compute the deflection: 1) Calculate the displacement for every image with respect to the position of the first image. In this case, no error is accumulated. This method should be used for small distances and high accuracy. 2) Compute the displacements between all successive images pairs. Possibility 2) should be used for large motion amplitudes because method 1) may produce absurd results in this case. The maximum amplitude for method 1) depends on the contrast of the images and the structure of the specimen and has to be found for every device by experiment. Usually method 1) is more accurate but less robust. If method 1) converges, it is the better choice. From our experience method 1) works fine up to 2 μm amplitude. The time needed to process the data shown in Fig. 7 is approximately 5 s when the optimization problem (6) is formulated using the translation method expressed by (11) and (12). One limitation on the methods we have described is that

the surfaces inspected may not slope by more than about 5° before errors resulting from parallax become significant; at a 5° slope the error is roughly 0.4%.

B. Algorithm for Out-of-Plane-Motion Computation

The in-plane-displacement data between the images is used to calculate the in-plane motions from the interferograms of *image set 2* with the image-translation method expressed by (11) and (12). This is necessary to make sure that out-of-plane deflection is computed in respect to points on the device surface. Otherwise the algorithm would compare different points on the surface to calculate deflection, which would be without value. After this procedure we use an algorithm that we have reported in detail in [5] and which we summarize in the following.

The data-evaluation software reads the gray-level distribution of the TIFF-images as a function

$$I_n(i, j) = A(i, j) + B(i, j) \cos(\varphi(i, j) + \alpha_n). \quad (14)$$

In (14), the term $\cos(\varphi(i, j) + \alpha_n)$ includes the phase function $\varphi(i, j)$. $\varphi(i, j)$ is the phase difference between measurement and reference beam at (i, j) resulting from the surface height of the specimen $h(i, j)$ and the phase shift $\alpha_n = 4\pi \cdot s/\lambda$ resulting from the position of the reference mirror. The functions $A(i, j)$ and $B(i, j)$ are governed by the spatial variations in amplitudes of the beams returned from the two interferometer arms and result from differences of the surface reflectivity.

To measure the shape of a static specimen or that of a moving specimen “frozen” by the strobe light we use phase-shifting interferometry (PSI) with five steps. The PSI algorithm calculates a wrapped-phase map following a method known as Hariharan’s Algorithm [19]. The algorithm calculates the wrapped phase $\phi(i, j)$ from the five intensity amplitudes $I_1(i, j) \cdots I_n(i, j) \cdots I_5(i, j)$ using the formula

$$\phi(i, j) = \arctan \left[\frac{2(I_2(i, j) - I_4(i, j))}{2I_3(i, j) - I_5(i, j) - I_1(i, j)} \right]. \quad (15)$$

Inputs to this algorithm should change phase by approximately $\pi/2$ in each data-acquisition step. The surface under test is assumed to be smooth and continuous; abrupt steps are removed by software.

A piezoelectric, translation stage (Polytec PI P-753.11C) moves the reference mirror with nanometer precision. During each measurement sequence the reference-mirror step is one eighth of the illuminating wavelength λ (86 nm for the 688 nm diode-laser wavelength) which results (through the beam reflection on the reference mirror) in the required phase-step size $\alpha_n - \alpha_{n-1} = \pi/2$. Thus, four mirror variations result in a phase shift of 2π in the two-dimensional function $\cos(\varphi(i, j) + \alpha_n)$ of the fringe pattern at the CCD sensor, as shown on Fig. 2. The fifth image should therefore be the same as the first image. When the reference mirror moves forward, the fringes move in the positive-gradient direction of the slope.

The Hariharan Algorithm [19] is relatively error-resistant (e.g., to errors caused by vibrations). For example an error of the reference-mirror step size of $s = 2$ nm leads to an error of 0.02 nm for the wrapped-height map $(\lambda \cdot \phi(i, j)/4\pi)$. Our single-wavelength system measures wave-front-phase modulo 2π and, therefore, calculates a “wrapped” phase

map from the interferogram sequence. The unwrapped phase map $\varphi(i, j) = \phi(i, j) + 2n(i, j)\pi$ is determined from the wrapped-phase function $\phi(i, j)$. The spatially varying integer $n(i, j)$ is present because the optical phase can only be measured modulo 2π in a single-wavelength interferometer. Finally, the surface-height map $h(i, j)$ can be found using

$$h(i, j) = \lambda \cdot \varphi(i, j) / 4\pi. \quad (16)$$

This procedure is repeated for different strobed-light delays Δt , corresponding to a strobed-light-phase delay $\gamma = 2\pi\nu_s \Delta t$, with ν_s the strobe frequency. In addition a time-unwrapping algorithm is employed to enable the system to measure pure piston motion.

IV. SMIS SPECIFICATION

The in-plane-profile resolution is the spatial resolution limited by the numerical aperture of the imaging optic and is approximately $1 \mu\text{m}$ if the microscope objective (f_m) is a $20\times$ objective. The in-plane-displacement resolution depends on the algorithm and has been investigated with a test image for different initial displacements. A steady object, the slider without any applied voltages, has been captured. No motion should be detected but the measurement in Fig. 4(a) shows a random deflection with maximum amplitude of $\pm 8 \text{ nm}$. This experiment shows the noise of the in-plane measurement.

The root-mean-square (*rms*)-value (root mean square) of this noise measurement is 3.6 nm . The noise can result from noise of the camera or from mechanical vibrations. The system can detect harmonic motion with an amplitude greater than the rms-value (3.6 nm). The resolution of the out-of-plane surface measurement is limited by imperfections in the optical elements and by dust in the optical path. The out-of-plane-profile repeatability is smaller than 5 nm [5]. The out-of-plane-profile resolution is limited through imperfections in the system optics and is approximately 25 nm . The rms-value of the measurement shown in Fig. 4(b) is 0.7 nm . This result was achieved by subtracting to surface profile measurements of a reference flat and by printing a cross line. The resolution for out-of-plane motion is 0.7 nm (minimum amplitude of a harmonic out-of-plane motion).

The time resolution of our system is defined by the width of the strobe pulse, and the precision of the measurement depends on the jitter in the strobe-phase delay. Constant delay and jitter are generated in every electronic device and should be calibrated. We took $n = 85$ measurements of the delay between a square MEMS-input pulse and the laser pulse when the delay δ at the delay generator was set to $\delta = 0 \mu\text{s}$. The averaged delay $\delta_{\text{err}} = 1/n \sum_{i=1}^n \delta_i$ was measured to be approximately $\delta_{\text{err}} = 427 \text{ ns}$. This error is taken into account by setting the corrected delay to $\delta_{\text{cor}} = \delta - \delta_{\text{err}}$ for $\delta > \delta_{\text{err}}$ in the software. For high frequencies ($\nu < 10 \text{ kHz}$) it is possible for a delay $\delta < \delta_{\text{err}}$ to be set. In this case we use the frequency scaler $\nu_r = 1/2\nu$. Then (if $\delta < \delta_{\text{err}}$), δ_{cor} is set to be $\delta_{\text{cor}} = 1/\nu - \delta_{\text{err}}$ automatically through our software. In this way, constant delays are considered in the software and, therefore, have a small influence

on the time accuracy. Problematic for the accuracy is the jitter δ_{jit} . The jitter is the standard deviation

$$\delta_{\text{jit}} = \sqrt{1/(n-1) \sum_{i=1}^n (\delta - \delta_{\text{err}})^2}.$$

We have measured the jitter of our electronic to be $\delta_{\text{jit}} = 28.9 \text{ ns}$.

In addition, the laser-pulse width defines the time resolution of our system because the laser pulse freezes the motion. The minimum width is 100 ns . To optimize the overshoot and the rise time we have chosen the series resistance on the laser mounting board (LPD-382P, ILX Lightwave) to be 2.5Ω .

V. EXPERIMENTS ON MEMS

A. Gimballed Microactuator

The gimballed microactuator, a multiple degree-of-freedom device, has been developed by Lilac Muller, Albert Pisano, and Roger Howe at BSAC. The microactuator is driven electrostatically by applying a constant voltage V_{dc} at the rotor of the device and a time-dependent voltage $V(t)$ at the stators. The production with the HEXSIL process and its functionality, the differential gap-closing drive, are all described in references [20] and [21]. A SEM photograph of the microactuator with an assembled read/write head is shown in Fig. 5. To demonstrate our combined in-plane and out-of-plane algorithm, we have measured the full three-dimensional motion of one single area on the slider surface for an harmonic input signal with a frequency of $\nu = 1.25 \text{ kHz}$, an amplitude of $V_m = 7.5 \text{ V}$ ($V(t) = V_m \sin(2\pi ft)$), and a dc voltage $V_{\text{DC}} = 16 \text{ V}$. The area on the device surface that has been investigated is marked in Fig. 5. The driving frequency of 1.24 kHz is out of the designed dynamic range of the actuator drive ($< 1 \text{ kHz}$) but close to a device mechanical resonance. The actuator is designed to perform pure in-plane motion, but through slight misalignment of the read/write head an energy transfer from in-plane mode to the out-of-plane modes is possible. We have investigated this effect.

Fig. 6 shows the frozen images of *set 1* at $\gamma = \pi/2$ (a) and $\gamma = 3\pi/2$ rad (b) strobe-phase delay in respect to the input signal. The displacement can clearly be seen in the zoomed region of interest. Altogether, 16 strobe-phase delays have been captured. The in-plane algorithm expressed by (11) and (12) is used to calculate the in-plane motion shown in Fig. 7. Fig. 8 shows two fringe-image sequences of *set 2* at $\gamma = 0$ rad and $\gamma = \pi$ rad strobe-phase delay. Every sequence of *set 2* shows five images for the same strobe-phase delay but for five different phase shifts α_n defined by the reference-mirror positions.

The in-plane displacement, which is also captured in the images of *set 2* is removed by the software using the data shown in Fig. 7 and by employing the image-translation method expressed through equations (11) and (12). After the in-plane displacement is removed, the surface profile and out-of-plane deflection is calculated with the algorithm expressed by (15) and (16). There is no bending in the investigated surface because

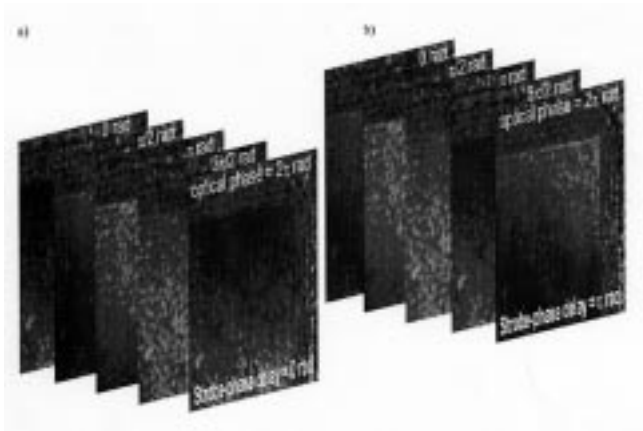


Fig. 8. Two sequences of set 2 for a stroke-phase delay ϕ of (a) 0 and (b) π rad.

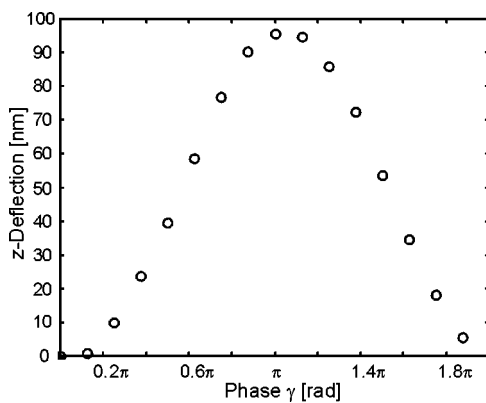


Fig. 9. Out-of-plane motion at 1250 kHz.

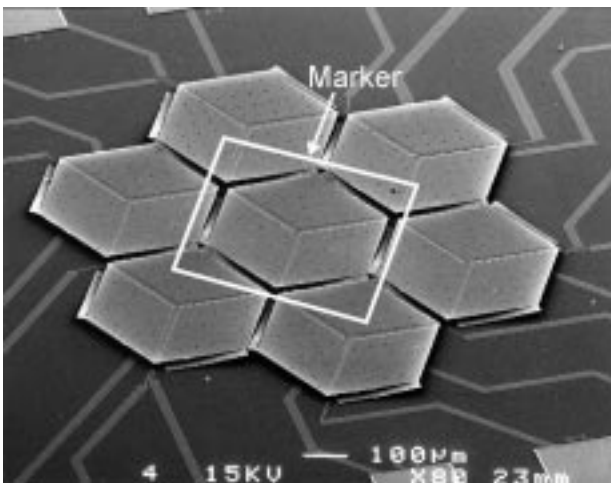


Fig. 10. SEM of a micromirror-actuator array (courtesy Michael Helmbrecht).

the slider is a rigid body. By performing a least-square optimization, a plane is fitted to every height map of the 16 investigated strobe phases and the z -displacement is computed. The worst-case-out-of-plane deflection is shown in Fig. 9.

B. Micromirror for Adaptive Optics

A second demonstration of the SMIS is to characterize the three-dimensional motion of a micromachined electrostatic actuator built for an adaptive-optics mirror array. This device has

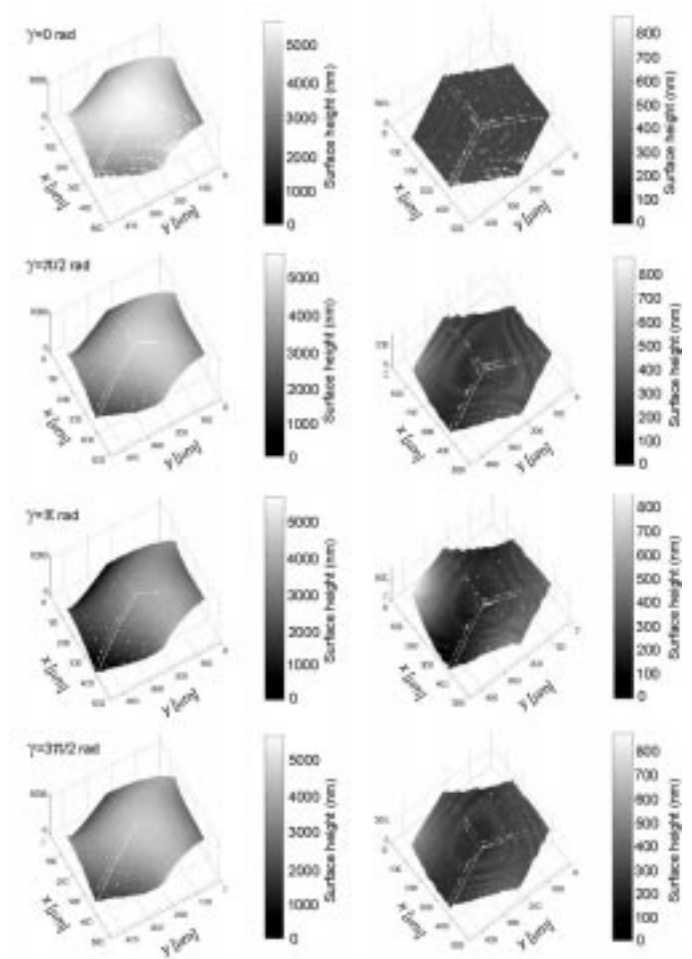


Fig. 11. (a) Measured mirror deflection and deformation and (b) mirror deformation after deflection has been removed mathematically.

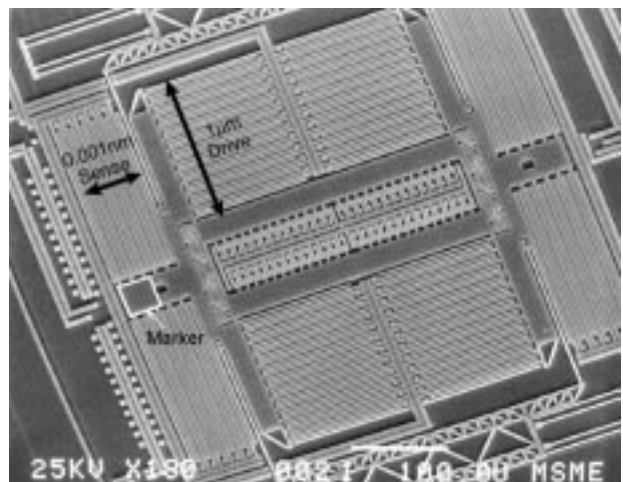


Fig. 12. SEM of a microgyroscope (courtesy Joe Seeger).

been developed by Helmbrecht *et al.* at BSAC. Fabrication and functionality are described in reference [22]. The actuator array, shown in the scanning electron micrograph (SEM) in Fig. 10, has been produced by surface micromachining. Each actuated mirror-support platform is lifted up by three bimorph cantilever beams. Electrostatic actuation allows both tilt and piston motions of the platforms. Flat single-crystal silicon mirrors are at-

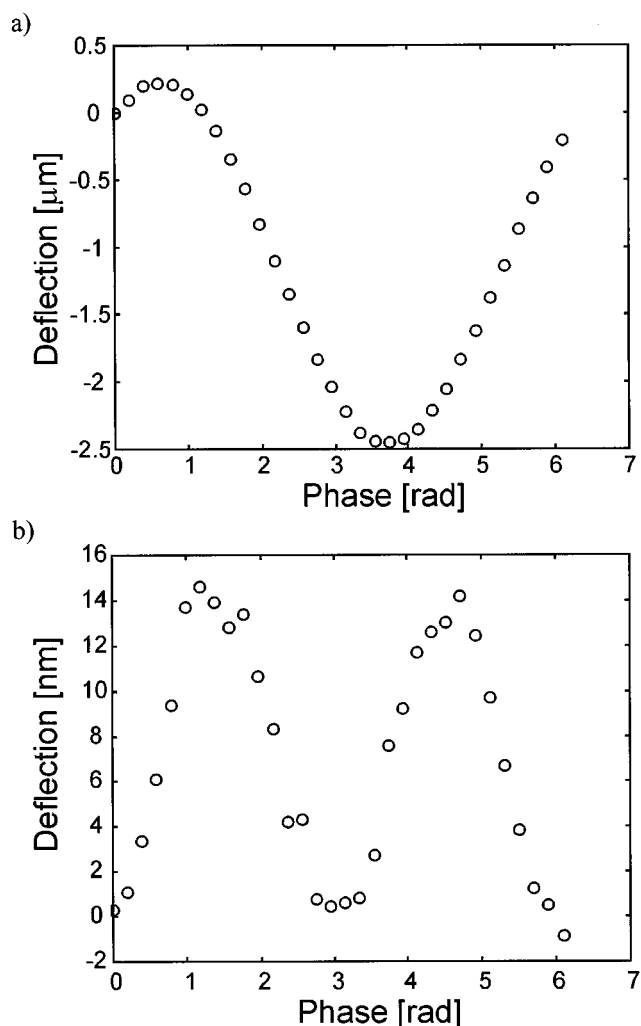


Fig. 13. (a) In-plane motion and (b) out-of-plane motion of measured surface.

tached to each of the support structures using a fluidic self-assembly technique developed by Srinivasan and Howe at BSAC [23]. The SMIS has been employed to investigate the dynamics of the actuator platforms under 1 kHz excitations resulting in the measurements shown in Fig. 11(a) which reveal displacements up to $5\ \mu\text{m}$ under 50 V drive. Higher order modes can be seen after tilt and piston terms have been removed mathematically as shown in Fig. 11(b). The in-plane motion detected for this device can be neglected for this application (amplitude $< 400\ \text{nm}$).

C. Gyroscope

A third example in which the SMIS has been used is to study a surface-micromachined gyroscope developed by Seeger, Jiang, and Boser at BSAC. The gyroscope was surface-micromachined using the Multi-User-MEMS-Process Service (MUMPS). The mechanical microstructure is integrated with the electronic circuits for processing of the measurement and driving signals for the proof mass. The mechanical structure is shown in the SEM photograph in Fig. 12. The microgyroscope measures rotations by exciting deflection of a proof mass and sensing the displacement in a sense direction that is perpendicular to it (see Fig. 12). The proof mass is driven electrostatically with gap-closing ac-

tuators. The microgyroscope is described in references [24] and [25].

We have studied the 3-D motions of the device at 9 kHz when it is driven from a TTL source at 4.5 V amplitude. The result of the in-plane motion in drive direction is shown in Fig. 13(a). A very small (7 nm) out-of-plane motion has been excited at twice the frequency of the in-plane motion [see Fig. 13(b)].

VI. CONCLUSION

We have presented a system for the 3-D dynamic characterization of micromechanical devices, the Stroboscopic Microscopic Interferometer System (SMIS). The SMIS can extract data at time intervals as short as 100 nanoseconds and measures full 3-D displacements with resolutions within 5 nm in surface dimensions and 0.7 nm for displacements perpendicular to the surface. The SMIS saves two sets of images on the computer hard disk. One set is a strobed, cinematographic image sequence used to compute in-plane motions. The other set contains interferograms that are used to compute the out-of-plane displacements of the surface during the strobe delay periods. Performance of the SMIS is demonstrated by study of the dynamic behavior of three disparate micromechanical devices: a micromachined electrostatically driven actuator for read/write heads in disk drives, actuator platforms to support an array of micromirrors for adaptive-optics applications, and a MEMS microgyroscope.

ACKNOWLEDGMENT

Discussion and experimental support by M. Helmbrecht, L. Muller, J. Seeger, and M. Young are gratefully acknowledged.

REFERENCES

- [1] P. Krehl *et al.*, "High-speed visualization, a powerful diagnostic tool for microactuators—Retrospect and prospect," *Microsyst. Technol.*, vol. 5, pp. 113–132, 1999.
- [2] MSV 300—Micro Scanning Vibrometer, "polytec PI product information," Tustin, CA.
- [3] R. A. Lawton *et al.*, "MEMS characterization using scanning laser vibrometer," in *Proc. SPIE 1999 Symp. Microelectronic Manufacturing*, 1999.
- [4] A. Klein *et al.*, "Transient measurement of surface deflection for beams and membranes in micromechanical devices," in *Proc. 2nd Int. Conf. on Vibration Measurements by Laser Techniques: Advances and Applications*, Ancona, Italy, 1998, pp. 618–623.
- [5] M. Hart *et al.*, "Stroboscopic interferometer system for dynamic MEMS characterization," *J. Microelectromech. Syst.*, vol. 9, pp. 409–418, 2000.
- [6] C. Rembe *et al.*, "Stroboscopic interferometer with variable magnification to measure dynamics in an adaptive-optics micromirror," in *Proc. IEEE Int. Conf. on Optical MEMS 2000*, Sheraton Kauai, Aug. 21–24, 2000, pp. 73–74.
- [7] C. Q. Davis *et al.*, "Statistics of subpixel registration algorithms based on spatiotemporal gradients or block matching," *Optical Engineering*, vol. 37, pp. 1290–1298, 1998.
- [8] C. Q. Davis *et al.*, "Using a light microscope to measure motions with nanometer accuracy," *Optic. Eng.*, vol. 37, pp. 1299–1304, 1998.
- [9] W. Hemmert *et al.*, "Nanometer resolution of three-dimensional motions using video interference microscopy," in *Proc. IEEE Int. MEMS 99*, Orlando, FL, Jan. 17–21, 1999.
- [10] C. Rembe, "Hochgeschwindigkeitskinematographie zur Diagnostik dynamischer Prozesse in der Mikrosystemtechnik," in *Fortschritt-Berichte VDI*. Düsseldorf, Germany: VDI Verlag, 1999.
- [11] C. Rembe *et al.*, "Investigations of nonreproducible phenomena in thermal ink jets with real high-speed-cine photomicrography," *J. Imag. Sci. Technol.*, vol. 43, pp. 325–331, 1999.

- [12] C. Rembe *et al.*, "Analysis of the dynamics in microactuators using high-speed cine photomicrography," *J. of Microelectromechanical Systems*, vol. 10, pp. 137–145, March 2001.
- [13] H. Riesenber, Ed., *Handbuch der Mikroskopie*. Berlin: VEB Verlag Technik, 1988.
- [14] D. Malacara, Ed., *Optical Shop Testing*, 2nd ed. New York: Wiley, 1992.
- [15] K. R. Castleman, *Digital Image Processing*. Upper Saddle River: Prentice Hall, 1996.
- [16] E. Walter *et al.*, *Identification of Parametric Models*. London, U.K.: Springer, 1997.
- [17] J. Nelder *et al.*, "A simplex method for function minimization," *Comput. J.*, vol. 7, pp. 308–313, 1964.
- [18] L. Brown, "A survey of image registration techniques," *ACM Comput. Surv.*, vol. 24, no. 4, pp. 325–376, 1992.
- [19] J. E. Greivenkamp *et al.*, "Phase shifting interferometers," *Optical Shop Testing*, pp. 501–598, 1992.
- [20] L. Muller, "Gimballed electrostatic microactuators with embedded interconnects," Ph.D. dissertation, Department of Mechanical Engineering, University of California, Berkeley, CA, 2000.
- [21] L. Muller *et al.*, "Electrical isolation process for molded high-aspect-ratio polysilicon microstructures," in *Proc. 13th Int. Workshop on Micro Electro Mechanical Systems (MEMS 2000)*, Miyazaki, Japan, Jan. 2000, pp. 590–595.
- [22] M. A. Helmbrecht *et al.*, "Micromirrors for adaptive-optics arrays," in *Proc. 11th Conference on Solid-State Sensors and Actuators—Transducers '01*, Munich, Germany, June 10–14, 2001, pp. 1290–1293.
- [23] U. Srinivasan *et al.*, "Microstructure to substrate self-assembly using capillary forces," *J. Microelectromech. Syst.*, vol. 10, pp. 17–24, 2001.
- [24] X. Jiang, J. I. Seeger, M. Kraft, and B. E. Boser, "A monolithic surface micromachined Z-axis gyroscope with digital output," in *2000 Symp. VLSI Circuits*, Honolulu, HI, June 15–17, 2000.
- [25] J. I. Seeger, X. Jiang, M. Kraft, and B. E. Boser, "Sense finger dynamics in a $\Sigma\Delta$ force-feedback gyroscope," in *2000 Solid-State Sensor and Actuator Workshop*, Hilton Head Island, SC, June 4–8, 2000.



Christian Rembe received the diploma of physics from the University of Hanover, Hanover, Germany, in 1994. From 1994 to 1999, he was a Ph.D. student at the University of Ulm, Ulm, Germany, where he received the Doctorate degree in electrical engineering.

In 1999, he joined the Berkeley Sensor and Actuator Center at the University of California, Berkeley, as Postdoctoral Research Engineer with support of a Feodor-Lynen-Scholarship of the Alexander von Humboldt-Foundation and a MacKay-Lecturer Fellowship. Since 2001, he has been Division Manager of Development Optics at Polytec GmbH, Waldbronn, Germany. For his work about high-speed visualization of dynamic processes in MEMS, he received the Promotionspreis (Ph.D. award) of the Ulmer Universitätsgesellschaft, and together with E. P. Hofer, the Landesforschungspreis (research award) 1999 of Baden-Württemberg for applied sciences.



Richard S. Muller (S'57–M'58–SM'70–F'88–LF'97) received the mechanical engineer degree from Stevens Institute of Technology, Hoboken, NJ, in 1955. He then entered California Institute of Technology, Pasadena, where he received the M.S. and Ph.D. degrees in electrical engineering and physics.

He worked in industry at Hughes Aircraft Company and joined the faculty at the University of California, Berkeley, in 1962, where his research focus was on the physics of integrated circuit devices. Together with Dr. T. I. Kamins of Hewlett-Packard Company, he first published *Device Electronics for Integrated Circuits* in 1977. A third edition of this book is being published in October 2003. In the late 1970s, he began research in the area now known as MEMS and, together with R. M. White, he founded the Berkeley Sensor & Actuator Center in 1986. He wrote the proposal to establish IEEE/ASME JOURNAL OF MICROELECTROMECHANICAL SYSTEMS (JMEMS) and is currently the Editor-in-Chief.

Dr. Muller is a Member of the U.S. National Academy of Engineering and has been awarded a career MEMS Award at TRANSDUCERS '97 as well as the IEEE Brunetti Award (1998 with R. T. Howe), a Fulbright Professorship, and a von Humboldt Research Award at TU Berlin, Germany, in 1994. His other awards include the Berkeley Citation and the Renaissance Award from Stevens Institute of Technology. He has been a Member of the National Materials Advisory Board and served on several National Research Council study panels as well as chairing a 1997 panel for which he acted as editor of a widely distributed report on the promises and challenges of MEMS. He presently serves on the Board of Trustees of Stevens Institute of Technology.